1   **Utsu aftershock productivity law explained from geometric operations on the**

2   **permanent static stress field of mainshocks**

3   Arnaud Mignan*

5   Institute of Geophysics, Swiss Federal Institute of Technology, Zurich

6   *Address:* ETHZ, Institute of Geophysics, NO H66, Sonneggstrasse 5, CH-8092 Zurich

8   *Correspondence to:* arnaud.mignan@sed.ethz.ch

10   *Abstract:* The aftershock productivity law is an exponential function of the form

11    $K \propto \exp(\alpha M)$ with K the number of aftershocks triggered by a given mainshock of

12   magnitude M and $\alpha \approx \ln(10)$ the productivity parameter. This law remains empirical

13   in nature although it has also been retrieved in static stress simulations. Here, we

14   parameterize this law using the Solid Seismicity Postulate (SSP), the basis of a

15   geometrical theory of seismicity where seismicity patterns are described by

16   mathematical expressions obtained from geometric operations on a permanent static

17   stress field. We first test the SSP that relates seismicity density to a static stress step

18   function. We show that it yields a power exponent $q = 1.96 \pm 0.01$ for the power-law

19   spatial linear density distribution of aftershocks, once uniform noise is added to the

20   static stress field, in agreement with observations. We then recover the exponential

21   function of the productivity law with a break in scaling obtained between small and

22   large M, with $\alpha = 1.5\ln(10)$ and $\ln(10)$, respectively, in agreement with results from

23   previous static stress simulations. Possible biases of aftershock selection, verified to

24   exist in Epidemic-Type Aftershock Sequence (ETAS) simulations, may explain the

25   lack of break in scaling observed in seismicity catalogues. The existence of the

26   theoretical kink remains however to be proven. Finally, we describe how to estimate

27   the Solid Seismicity parameters (activation density δ_+, aftershock solid envelope r_*

28   and background stress amplitude range Δo_*) for large M values.

29

30   **1. Introduction**

31   Aftershocks, one of the most studied patterns observed in seismicity, are

32   characterized by three empirical laws, which are functions of time, such as the

33   Modified Omori law (e.g., Utsu et al., 1995), space (e.g., Richards-Dinger et al., 2010;

34   Moradpour et al., 2014), and mainshock magnitude (Utsu, 1970a; b; Ogata, 1988).

35 The present study focuses on the latter relationship, i.e., the Utsu aftershock

36 productivity law, which describes the total number of aftershocks K produced by a

37 mainshock of magnitude M as

38 $$K(M) = K_0 \exp[\alpha(M - m_0)] \tag{1}$$

39 with m_0 the minimum magnitude cutoff (Utsu, 1970b; Ogata, 1988). This relationship

40 was originally proposed by Utsu (1970a; b) by combining two other empirical laws,

41 the Gutenberg-Richter relationship (Gutenberg and Richter, 1944) and Båth's law

42 (Båth, 1964), respectively:

43 $$\begin{cases} N(\geq m) = A\exp[-\beta(m - m_0)] \\ \quad N(\geq M - \Delta m_B) = 1 \end{cases} \tag{2}$$

44 with N the number of events above magnitude m, A a seismic activity constant, β the

45 magnitude size ratio (or $b = \beta/\ln(10)$ in base-10 logarithmic scale) and Δm_B the

46 magnitude difference between the mainshock and its largest aftershock, such that

47 $$K(M) = N(\geq m_0|M) = \exp(-\beta\Delta m_B)\exp[\beta(M - m_0)] \tag{3}$$

48 with $K_0 = \exp(-\beta\Delta m_B)$ and $\alpha \equiv \beta$. Eq. (3) was only implicit in Utsu (1970a) and

49 not exploited in Utsu (1970b) where K_0 was fitted independently of the value taken by

50 Båth's parameter Δm_B. The α-value was in turn decoupled from the β–value in later

51 studies (e.g., Seif et al. (2017) and references therein).

52   Although it seems obvious that Eq. (1) can be explained geometrically if the

53 volume of the aftershock zone is correlated to the mainshock surface area S with

54 $$S(M) = 10^{M-4} = \exp[\ln(10)(M - 4)] \tag{4}$$

55 (Kanamori and Anderson, 1975; Yamanaka and Shimazaki, 1990; Helmstetter, 2003),

56 there is so far no analytical, physical expression of Eq. (1) available. Although Hainzl

57 et al. (2010) retrieved the exponential behavior in numerical simulations where

58 aftershocks were produced by the permanent static stress field of mainshocks of

59   different magnitudes, it remains unclear how K_0 and α relate to the underlying

60   physical parameters.

61   The aim of the present article is to describe the Utsu aftershock productivity

62   equation (Eq. 1) in terms of a geometrical theory of seismicity coined "Solid

63   Seismicity", where the Eq. (4) scaling is parameterized using the Solid Seismicity

64   Postulate (SSP). The SSP has already been shown to effectively explain other

65   empirical laws of both natural and induced seismicity from simple geometric

66   operations on a permanent static stress field (Mignan, 2012; 2016a). The theory is

67   applied here for the first time to describe aftershocks.

68

69   **2. Physical Expression of the Aftershock Productivity Law**

70   *2.1. Demonstration of the productivity law by geometric operations*

71   "Solid Seismicity", a geometrical theory of seismicity, is based on the

72   following Postulate (Mignan et al., 2007; Mignan, 2008, 2012; 2016a):

73

74   **Solid Seismicity Postulate (SSP):** *Seismicity can be strictly categorized*

75   *into three regimes of constant spatiotemporal densities δ – background*

76   *δ_0, quiescence δ_- and activation δ_+ (with $\delta_- \ll \delta_0 \ll \delta_+$) - occurring*

77   *respective to the static stress step function:*

$$\delta(\sigma) = \begin{cases} \delta_- & , \sigma < -\Delta o_* \\ \delta_0 & , \sigma \leq |\pm\Delta o_*| \\ \delta_+ & , \sigma > \Delta o_* \end{cases} \qquad (5)$$

79   *with σ the static stress [stress unit], Δo_* the background stress amplitude*

80   *range [stress unit], a stress threshold value separating two seismicity*

81   *regimes, and δ the spatial density of events [number of events per unit of*

82   *volume] per seismicity regime.*

83

84   We mean by "strictly categorized" that any seismicity population is either part of the

85   background, quiescence or activation regime (or class), with no other regime/class

86   possible (i.e., a sort of hard labelling). Based on this Postulate, Mignan (2012)

87   demonstrated the power-law behavior of precursory seismicity in agreement with the

88   observed time-to-failure equation (Varnes, 1989), while Mignan (2016a)

89   demonstrated both the observed parabolic spatiotemporal front and the linear

90   relationship with injection-flow-rate of induced seismicity (Shapiro and Dinske,

91   2009). It remains unclear whether the SSP has a physical origin or not. If not, it would

92   still represent a reasonable approximation of the linear relationship between event

93   production and static stress field in a simple clock-change model (Hainzl et al., 2010;

94   Fig. 1a). For the testing of the SSP on the observed spatial distribution of aftershocks,

95   see section 2.2. The power of Eq. (5) is that it allows defining seismicity patterns in

96   terms of "solids" described by the spatial envelope $r_* = r(\sigma = \pm\Delta o_*)$ where r is the

97   distance from the static stress source (e.g., mainshock rupture) and r_* the distance r at

98   which there is a change of regime (quiescence/background at $\sigma = -\Delta o_*$ or

99   background/activation at $\sigma = \Delta o_*$). The spatiotemporal rate of seismicity is then a

100   mathematical expression defined by the density of events δ times the volume

101   characterized by r_* (see previous demonstrations in Mignan et al. (2007) and Mignan

102   (2011; 2012; 2016a) where simple algebraic expressions were obtained).

103   In the case of aftershocks, we define the static stress field of the mainshock by

104   $$\sigma(r) = -\Delta\sigma_0 \left[\left(1 - \frac{c^3}{(r+c)^3}\right)^{-1/2} - 1 \right] \tag{6}$$

105   with $\Delta\sigma_0 < 0$ the mainshock stress drop, c the crack radius and r the distance from the

106   crack. Eq (6) is a simplified representation of stress change from slip on a planar

107 surface in a homogeneous elastic medium. It takes into account both the square root

108 singularity at crack tip and the $1/r^3$ falloff at higher distances (Dieterich, 1994; Fig.

109 1b). It should be noted that this radial static stress field does not represent the

110 geometric complexity of Coulomb stress fields (Fig. 2a). However we are here only

111 interested in the general behavior of aftershocks with Eq. (6) retaining the first-order

112 characteristics of this field (i.e., on-fault seismicity; Fig. 2b), which corresponds to the

113 case where the mainshock relieves most of the regional stresses and aftershocks occur

114 on optimally oriented faults. It is also in agreement with observations, most

115 aftershocks being located on and around the mainshock fault traces in Southern

116 California (Fig. 2c; see section "Observations & Model Fitting"). The occasional

117 cases where aftershocks occur off-fault (e.g., Ross et al., 2017) can be explained by

118 the mainshock not relieving all of the regional stress (King et al., 1994; Fig. 2d).

119   For $r_* = r(\sigma = \Delta o_*)$, Eq. (6) yields the aftershock solid envelope of the form:

120
$$r_*(c) = \left\{ \frac{1}{\left[1 - \left(1 - \frac{\Delta\sigma_*}{\Delta\sigma_0}\right)^{-2}\right]^{1/3}} - 1 \right\} c = Fc, \tag{7}$$

121 function of the crack radius c and of the ratio between background stress amplitude

122 range Δo_* and stress drop $\Delta\sigma_0$ (Fig. 1c). With $\Delta\sigma_0$ independent of earthquake size

123 (Kanamori and Anderson, 1975; Abercrombie and Leary, 1993) and Δo_* assumed

124 constant, r_* is directly proportional to c with proportionality constant, or stress factor,

125 F (Eq. 7). Geometrical constraints due to the seismogenic layer width w_0 then yield

126
$$c(M) = \begin{cases} \left(\frac{S(M)}{\pi}\right)^{1/2} & , S(M) \leq \pi w_0^2 \\ w_0 & , S(M) > \pi w_0^2 \end{cases} \tag{8}$$

127 with S the rupture surface area defined by Eq. (4) and c becoming an effective crack

128 radius (Kanamori and Anderson, 1975; Fig. 1d). Note that the factor of 2 (i.e., using

129   w_0 instead of $w_0/2$) comes from the free surface effect (e.g., Kanamori and Anderson,

130   1975; Shaw and Scholz, 2001).

131   The aftershock productivity $K(M)$ is then the activation density δ_+ times the

132   volume $V_*(M)$ of the aftershock solid. For the case in which the mainshock relieves

133   most of the regional stress, stresses are increased all around the rupture (King et al.,

134   1994), which is topologically identical to stresses increasing radially from the rupture

135   plane (Fig. 2a-b). It follows that the aftershock solid can be represented by a volume

136   of contour $r_*(M)$ from the rupture plane geometric primitive, i.e., a disk or a

137   rectangle, for small and large mainshocks, respectively. This is illustrated in Figure

138   3a-b and can be generalized by

139    $$V_*(M) = 2r_*(M)S(M) + \frac{\pi}{2}r_*^2(M)d \tag{9}$$

140   where d is the distance travelled around the geometric primitive by the geometric

141   centroid of the semi-circle of radius $r_*(M)$ (i.e., Pappus's Centroid Theorem), or

142    $$d = \begin{cases} 2\pi\left(c(M) + \frac{4}{3\pi}r_*(M)\right) & , c(M) + r_*(M) \leq \frac{w_0}{2} \\ 2w_0 & , c(M) + r_*(M) > \frac{w_0}{2} \end{cases} \tag{10}$$

143   For the disk, the volume (Eq. 9) corresponds to the sum of a cylinder of radius $c(M)$

144   and height $2r_*(M)$ (first term) and of half a torus of major radius $c(M)$ and minus

145   radius $r_*(M)$ (second term). For the rectangle, the volume is the sum of a cuboid of

146   length $l(M)$ (i.e., rupture length), width w_0 and height $2r_*(M)$ (first term) and of a

147   cylinder of radius $r_*(M)$ and height w_0 (second term; see red and orange volumes,

148   respectively, in Figure 3a-c). Finally inserting Eqs. (7), (8) and (10) into (9), we

149   obtain

150 $$K(M) = \delta_+ \begin{cases} \left[\frac{2F}{\sqrt{\pi}} + F^2\sqrt{\pi}\left(1 + \frac{4}{3\pi}F\right)\right]S^{3/2}(M) & , S(M) \leq \left(\frac{w_0\sqrt{\pi}}{2(1+F)}\right)^2 \\ \frac{2F}{\sqrt{\pi}}S^{3/2}(M) + F^2w_0S(M) & \left(\frac{w_0\sqrt{\pi}}{2(1+F)}\right)^2 < S(M) \leq \pi w_0^2 \\ 2Fw_0S(M) + \pi F^2w_0^3 & , S(M) > \pi w_0^2 \end{cases}$$

151   (11)

152   which is represented in Figure 3d. Considering the two main regimes only (small

153   versus large mainshocks) and inserting Eq. (4) into (11), we get

154 $$K(M) = \delta_+ \begin{cases} \left[\frac{2F}{\sqrt{\pi}} + F^2\sqrt{\pi}\left(1 + \frac{4}{3\pi}F\right)\right]\exp\left[\frac{3\ln(10)}{2}(M-4)\right] & , \text{small } M \\ 2Fw_0\exp[\ln(10)(M-4)] + \pi F^2w_0^3 & , \text{large } M \end{cases} \quad (12)$$

155   which is a closed-form expression of the same form as the original Utsu productivity

156   law (Eq. 1). Note that K and δ_+ are both, implicitly, function of the selected minimum

157   aftershock magnitude threshold m_0.

158   Here, we predict that the α-value decreases from $3\ln(10)/2 \approx 3.45$ to $\ln(10) \approx$

159   2.30 when switching regime from small to large mainshocks (or from 1.5 to 1 in base-

160   10 logarithmic scale). It should be noted that Hainzl et al. (2010) observed the same

161   break in scaling in static stress transfer simulations, which corroborates our analytical

162   findings. Hainzl et al. (2010) simulated aftershocks using the clock-change model

163   where events were advanced in time by the static stress change produced by a

164   mainshock in a three-dimensional medium. They explained the scaling break

165   observed in simulation as a transition from 3D to 2D scaling regime when the

166   mainshock rupture dimension approached w_0, which is compatible with the present

167   demonstration. For large M, the scaling is fundamentally the same as in Eq. (4). Since

168   that relation also explains the slope of the Gutenberg-Richter law (see physical

169   explanation given by Kanamori and Anderson,1975), it follows that $\alpha \equiv \beta$, which is

170   also in agreement with the original formulation of Utsu (1970a; b; Eq. 3).

171

 2.2. Testing of the SSP on the aftershock spatial distribution

173   The SSP predicts a step-like behavior of the aftershock spatial density for an

174   idealized smooth static stress field (Fig. 4a-b), which is in disagreement with real

175   aftershock observations. A number of studies have shown that the spatial linear

176   density distribution of aftershocks ρ is well represented by a power-law, expressed as

177   $\rho(r) \propto r^{-q}$ (13)

178   with *r* the distance from the mainshock and *q* the power-law exponent. This parameter

179   ranges over $1.3 \leq q \leq 2.5$ (Felzer and Brodsky, 2006; Lipiello et al., 2009; Marsan and

180   Lengliné, 2010; Richards-Dinger et al., 2010; Shearer, 2012; Gu et al., 2013;

181   Moradpour et al., 2014; van der Elst and Shaw, 2015). Although Felzer and Brodsky

182   (2004) suggested a dynamic stress origin for aftershocks, their results were later on

183   questioned by Richards-Dinger et al. (2010). Most of the studies cited above suggest

184   that the *q*-value is explained from a static stress process. As for the examples of

185   aftershocks shown to be dynamically triggered (e.g., Fan and Shearer, 2016), they are

186   too few to alter the aftershock productivity law and too remote to be consistently

187   defined as aftershocks in cluster methods.

188   In a more realistic setting, the static stress field must be heterogeneous (due to

189   the occurrence of previous events and other potential stress perturbations). We

190   therefore simulate the static stress field by adding a uniform random component

191   bounded over $\pm \Delta o_*$ following Mignan (2011) (see also King and Bowman, 2003).

192   Note that any deviation above Δo_* would be flattened to Δo_* over time by temporal

193   diffusion (so-called "historical ghost static stress field" in Mignan, 2016a). Figure 4c

194   shows the resulting stress field and Figure 4d the predicted aftershock spatial density.

195   Adding uniform noise blurs the contour of the aftershock solid, switching the

196   aftershock spatial density from a step function (Fig. 4b) to a power-law (Fig. 4d). We

197 fit Eq. (13) to the simulated data using the Maximum Likelihood Estimation (MLE)

198 method with $r_{min} = r_*$ (Clauset et al., 2009) and find $q = 1.96\pm0.01$, in agreement with

199 the aftershock literature. This result alone is however insufficient to prove the validity

200 of the SSP.

201

202 **3. Observations & Model Fitting**

203 *3.1. Data*

204   We consider the case of Southern California and extract aftershock sequences

205 from the relocated earthquake catalog of Hauksson et al. (2012) defined over the

206 period 1981-2011, using the nearest-neighbor method (Zaliapin et al., 2008; used with

207 its standard parameters originally calibrated for Southern California, considering only

208 the first aftershock generation). Only events with magnitudes greater than $m_0 = 2.0$ are

209 considered (a conservative estimate following results of Tormann et al. (2014);

210 saturation effects immediately after the mainshock are negligible when considering

211 entire aftershock sequences; Helmstetter et al., 2005).

212

213 *3.2. Aftershock spatial density distribution*

214   Figure 5a represents the spatial linear density distribution of aftershocks $\rho(r)$

215 for the four largest strike-slip mainshocks in Southern California: 1987 *M=6.6*

216 Superstition Hills, 1992 *M=7.3* Landers, 1999 *M=7.1* Hector Mine, and 2010 *M=7.2*

217 El Mayor. The distance between mainshock and aftershocks is calculated as

218 $r = \sqrt{(x - x_0)^2 + (y - y_0)^2}$ with (x, y) the aftershock coordinates and (x_0, y_0) the

219 coordinates of the nearest point to the mainshock fault rupture (as depicted in Figure

220 2c). The dashed black lines shown in Figure 5a are visual guides to $q = 1.96$, showing

221 that the SSP is compatible with real aftershock observations.

222   Comparing Figure 5a to Figure 4d suggests that r_* can be roughly estimated

223   from the spatial linear density plot, being the maximum distance r at which the

224   plateau ends, here leading to $r_* \approx 1$ km. This parameter is constant for different large

225   M values since both w_0 and $\Delta\sigma_0$ are constant while $\Delta\sigma_*$ is also *a priori* a constant. We

226   can then estimate the ratio $\Delta\sigma_*/\Delta\sigma_0$ from Eq. (7). However the result is ambiguous

227   due to uncertainties on the width w_0. For $w_0 = \{5, 10, 15\}$ km, we get $\Delta\sigma_*/\Delta\sigma_0 =\{$-

228     $0.54, -1.01, -1.38\}$.

229   As for the plateau value $\rho(r < r_*)$, it provides an estimate of the aftershock

230   activation density δ_+ with

231     $$\delta_+ = \frac{\rho(M, r < r_*)}{\exp[\ln(10)(M-4)]} \tag{14}$$

232   a volumetric density, i.e. the linear density ρ normalized by the mainshock rupture

233   area (Eq. 4). Due to the fluctuations in $\rho(r < r_*)$, δ_+ will be estimated from the

234   productivity law instead (see section 3.3) and $\rho(r < r_*)$ then estimated from Eq. (14)

235   (horizontal dashed colored lines), as detailed below.

236   It should be noted that we consider only the first-generation aftershocks to

237   avoid ρ heterogeneities from secondary aftershock clusters occurring off-fault. An

238   example of such heterogeneity/anisotropy is illustrated by the Landers-Big Bear case

239   (Fig. 2c; dotted colored curve on Fig. 5a). Those cases are not systematic and

240   therefore not considered in the aftershock productivity law. However they are also

241   due to static stress changes (e.g., King et al., 1994) with the anisotropic effects

242   explainable by Solid Seismicity through the concept of "historical ghost static stress

243   field" (Mignan, 2016a).

244

245   *3.3. Aftershock productivity law*

246   The observed number n of aftershocks of magnitude $m \geq m_0$ produced by a

247   mainshock of magnitude M (for a total of N mainshocks) in Southern California is

248   shown in Figures 5b (for large $M \geq 6$) and 6a (for the full range $M \geq m_0$). We fit Eq.

249   (1) to the data using the MLE method with the log-likelihood function

250    $LL(\theta; X = \{n_i; i = 1, ..., N\}) = \sum_{i=1}^{N}[n_i\ln[K_i(\theta)] - K_i(\theta) - \ln(n_i!)]$ (15)

251   for a Poisson process, representing the stochasticity of the count K of aftershocks

252   produced by a mainshock at any given time. Inserting Eq. (1) in Eq. (15) yields

253    $LL(\theta = \{K_0, \alpha\}; X) = \ln(K_0) \sum_{i=1}^{N} n_i + \alpha \sum_{i=1}^{N}[n_i(M_i - m_0)] - K_0 \sum_{i=1}^{N} \exp[\alpha(M_i - $

254    $m_0)] - \sum_{i=1}^{N} \ln(n_i!)$ (16)

255   (note that the last term can be set to 0 during LL maximization). For Southern

256   California, we obtain $\alpha_{MLE} = 2.32$ (1.01 in $\log_{10}$ scale) and $K_0 = 0.025$ when

257   considering large $M \geq 6$ mainshocks only to avoid the issues of scaling break and data

258   dispersion at lower magnitudes. This result, represented by the black solid line on

259   Figure 5b, is in agreement with previous studies in the same region (e.g., Helmstetter,

260   2003; Helmstetter et al., 2005; Zaliapin and Ben-Zion, 2013; Seif et al., 2017) and

261   with $\alpha = \ln(10) \approx 2.30$ predicted for large mainshocks in Solid Seismicity (Eq. 12).

262   Moreover we find a bulk $\beta_{MLE} = 2.34$ (1.02 in $\log_{10}$ scale) (Aki, 1965), in agreement

263   with $\alpha \equiv \beta$.

264   Let us now rewrite the Solid Seismicity aftershock productivity law (Eq. 12)

265   by only considering the large M case and injecting $r_* = Fw_0$ (by combining Eqs. 7-8).

266   We get

267    $K(M > M_{break}) = \delta_+\{2r_*\exp[ln(10)(M - 4)] + \pi r_*^2 w_0\}$ (17)

268   The role of w_0 is illustrated in Figure 5b for different values (dashed and dotted

269   curves) and shown to be insignificant for large M values. Therefore Eq. (17) can be

270   approximated to

271 $$K(M > M_{break}) \approx 2\delta_+ r_* \exp[ln(10)(M - 4)] \qquad (18)$$

272 By analogy with Eq. (1), we get

273 $$\delta_+ = \frac{K_0 \exp[\ln(10)(4-m_0)]}{2r_*} \qquad (19)$$

274 With $r_* \approx 1$ km estimated from $\rho(r)$ (section 3.2) and $K_0 = 0.025$, we obtain $\delta_+ = 1.23$

275 events/km^3 for $m_0 = 2$. We then get back the plateau $\rho(r < r_*)$ for different M values

276 from Eq. (14), as shown in Figure 5a (horizontal dashed colored lines). Although

277 based on limited data, this result suggests that the activation parameter δ_+ is constant

278 (at least for large M) in Southern California. Note that if $\rho(r < r_*)$ was well

279 constrained, it could have been estimated jointly with r_* from Figure 5a to predict the

280 aftershock productivity law of Figure 5b without further fitting required (hence

281 removing K_0 from the equation, K_0 having no physical meaning in Solid Seismicity).

282

283 **4. Role of aftershock selection on productivity scaling-break**

284 We tested the following piecewise model to identify any break in scaling at

285 smaller M, as predicted by Eq. (12):

286 $$K(M) = \begin{cases} K_0 \dfrac{\exp[\ln(10)(M_{break}-m_0)]}{\exp\left[\frac{3}{2}\ln(10)(M_{break}-m_0)\right]} \exp\left[\frac{3}{2}\ln(10)(M - m_0)\right] & , M \leq M_{break} \\ K_0 \exp[\ln(10)(M - m_0)] & , M > M_{break} \end{cases}$$

287 (20)

288 but with the best MLE result obtained for $M_{break} = m_0$, suggesting no break in scaling

289 in the aftershock productivity data, as observed in Figure 6a. Final parameter

290 estimates are $\alpha_{MLE} = 1.95$ (0.85 in $\log_{10}$ scale) and $K_0 = 0.141$ for the full mainshock

291 magnitude range $M \geq m_0$ (dotted line), subject to high scattering at low M values.

292 We now identify whether the lack of break in scaling in aftershock

293 productivity observed in earthquake catalogues could be an artefact related to the

294   aftershock selection method. We run Epidemic-Type Aftershock Sequence (ETAS)

295   simulations (Ogata, 1988; Ogata and Zhuang, 2006), with the seismicity rate

296
$$\begin{cases} \lambda(t,x,y) = \mu(t,x,y) + \sum_{i:t_j<t} K(M_i)f(t-t_i)g(x-x_i,y-y_i|M_i) \\ \qquad\qquad f(t) = c^{p-1}(p-1)(t+c)^{-p} \\ g(x,y|M) = \frac{1}{\pi}\big(de^{\gamma(M-m_0)}\big)^{q-1}\big(x^2+y^2+de^{\gamma(M-m_0)}\big)^{-q}(q-1) \end{cases} \tag{21}$$

297   Aftershock sequences are defined by power laws, both in time and space (for an

298   alternative temporal function, see Mignan (2015; 2016b); the spatial power-law

299   distribution is in agreement with Solid Seismicity in the case of a heterogeneous static

300   stress field – see section 2.2). μ is the Southern California background seismicity, as

301   defined by the nearest-neighbor method (with same t, x, y and m). We fix the ETAS

302   parameters to $\theta = \{c = 0.011$ day, $p = 1.08$, $d = 0.0019$ km^2, $q = 1.47$, $\gamma = 2.01$, $\beta =$

303   2.29, $K_0 = 0.08\}$, following the fitting results of Seif et al. (2017) for the Southern

304   California relocated catalog and $m_0 = 2$ (see their Table 1). However, we define the

305   productivity function $K(M)$ from Eq. (20) with $M_{break} = 5$. Examples of ETAS

306   simulations are shown in Figure 6b for comparison with the observed Southern

307   California time series. Figure 6c allows us to verify that the simulated aftershock

308   productivity is kinked at M_{break}, as defined by Eq. (20).

309   We then select aftershocks from the ETAS simulations with the nearest-

310   neighbor method. Figure 4d represents the estimated aftershock productivity, which

311   has lost the break in scaling originally implemented in the simulations (with an

312   underestimated $\alpha_{MLE} = 2.07$ as observed in the real case for $M \geq m_0$). Note that a

313   similar result is obtained when using a windowing method (Gardner and Knopoff,

314   1974). This demonstrates that the theoretical break in scaling predicted in the

315   aftershock productivity law can be lost in observations due to an aftershock selection

316   bias, all declustering techniques assuming continuity over the entire magnitude range.

317   While such a bias is possible, it yet does not prove that the break in scaling exists. The

318 fact that a similar break in scaling was obtained in independent Coulomb stress

319 simulations (Hainzl et al., 2010) however provides high confidence in our results.

320   One other possible explanation for lack of scaling break is that our

321 demonstration assumes moment magnitudes while the Southern California catalogue

322 is in local magnitudes. Deichmann (2017) demonstrated that while $M_L \propto M_w$ at large

323 M, $M_L \propto 1.5M_w$ at smaller M values. This could in theory cancel the kink in real data.

324 However the scaling break predicted by Deichmann (2017) occurs at several

325 magnitude units below the geometric scaling break expected by Solid Seismicity,

326 invalidating this second option for mid-range magnitudes M.

327

328 **5. Conclusions**

329   In the present study, a closed-form expression defined from geometric and

330 static stress parameters was proposed (Eq. 12) to describe the empirical Utsu

331 aftershock productivity law (Eq. 1). This demonstration is similar to the previous ones

332 made by the author to explain precursory accelerating seismicity and induced

333 seismicity (Mignan, 2012; 2016b), In all these demonstrations, the main physical

334 parameters remain the same, i.e. the activation density δ_+ (also δ_- and δ_0), the

335 background stress amplitude range Δo_*, and the solid envelope r_* which describes the

336 geometry of the "seismicity solid" (Fig. 3a-b). Further studies will be needed to

337 evaluate whether the δ_+ and Δo_* parameters are universal or region-specific and if the

338 same values apply to different types of seismicity at a same location.

339   Although the Solid Seismicity Postulate (SSP) (Eq. 5) remains to be proven, it

340 is so far a rather convenient and pragmatic assumption to determine the physical

341 parameters that play a first-order role in the behavior of seismicity. The similarity of

342 the SSP-simulated and observed values of the power-law exponent q of the aftershock

343 spatial density distribution shows that the SSP is consistent with large aftershock

344 observations once uniform noise is added to the stress field (Figs. 4d-5a). The impact

345 of other types of noise on q has yet to be investigated. The SSP is also complementary

346 to the more common simulations of static stress loading (King and Bowman, 2003)

347 and static stress triggering (Hainzl et al., 2010).

348 Analytic geometry, providing both a visual representation and an analytical

349 expression of the problem at hand (Fig. 3), represents a new approach to try to better

350 understand the behavior of seismicity. Its current limitation in the case of aftershock

351 analysis consists in assuming that the static stress field is radial and described by Eq.

352 (6) (e.g., Dieterich, 1994), which is likely only valid for mainshocks relieving most of

353 the regional stresses and with aftershocks occurring on optimally oriented faults (King

354 et al., 1994). More complex, second-order, stress behaviors might explain part of the

355 scattering observed around Eq. (1) (Fig. 6a), such as overpressure due to trapped high-

356 pressure gas for example (Miller et al., 2004 – see also Mignan (2016a) for an

357 overpressure field due to fluid injection). Other $\sigma(r)$ formulations could be tested in

358 the future, the only constraint on generating so-called seismicity solids being the use

359 of the postulated static stress step function of Eq. (5) (i.e., the Solid Seismicity

360 Postulate, SSP).

361 Finally, the disappearance of the predicted scaling break in the aftershock

362 productivity law once declustering is applied (Fig. 6) indicates that more work is

363 required in that domain. Only a declustering technique that does not dictate a constant

364 scaling at all M will be able to identify rather a scaling break really exists or not.

365

366 *Acknowledgments:* I thank N. Wetzler and two anonymous reviewers, as well as

367 editor Ilya Zaliapin, for their valuable comments.

368

References

370 Abercrombie, R. and Leary, P.: Source parameters of small earthquakes recorded at
371   2.5 km depth, Cajon Pass, Southern California: Implications for earthquake
372   scaling, Geophys. Res. Lett., 20, 1511-1514, 1993.

373 Aki, K.: Maximum Likelihood Estimate of b in the Formula log N = a-bM and its
374   Confidence Limits, Bull. Earthq. Res. Instit., 43, 237-239, 1965.

375 Båth, M.: Lateral inhomogeneities of the upper mantle, Tectonophysics, 2, 483-514,
376   1965.

377 Clauset, A., Shalizi, C. R. and Newman, M. E. J.: Power-Law Distributions in
378   Empirical Data, SIAM Review, 51, 661-703, doi: 10.1137/070710111, 2009.

379 Deichmann, N.: Theoretical Basis for the Observed Break in M_L/M_w Scaling between
380   Small and Large Earthquakes, Bull. Seismol. Soc. Am., 107, doi:
381   10.1785/0120160318, 2017.

382 Dieterich, J.: A constitutive law for rate of earthquake production and its application
383   to earthquake clustering, J. Geophys. Res., 99, 2601-2618, 1994.

384 Fan, W. and Shearer, P. M.: Local near instantaneously dynamically triggered
385   aftershocks of large earthquakes, Science, 353, 1133-1136, 2016.

386 Felzer, K. R. and Brodsky, E. E.: Decay of aftershock density with distance indicates
387   triggering by dynamic stress, Nature, 441, 735-738, doi: 10.1038/nature04799,
388   2006.

389 Gardner, J. K. and Knopoff, L.: Is the sequence of earthquakes in Southern California,
390   with aftershocks removed, Poissonian?, Bull. Seismol. Soc. Am., 64, 1363-1367,
391   1974.

392   Gu, C., Schumann, A. Y., Baisesi, M. and Davidsen, J.: Triggering cascades and

393   statistical properties of aftershocks, J. Geophys. Res. Solid Earth, 118, 4278-4295,

394   doi: 10.1002/jgrb.50306, 2013.

395   Gutenberg, B. and Richter, C. F.: Frequency of earthquakes in California, Bull.

396   Seismol. Soc. Am., 34, 185-188, 1944.

397   Hainzl, S., Brietzke, G. B. and Zöller, G.: Quantitative earthquake forecasts resulting

398   from static stress triggering, J. Geophys. Res., 115, B11311, doi:

399   10.1029/2010JB007473, 2010.

400   Hauksson, E., Yang, W. and Shearer, P. M.: Waveform Relocated Earthquake Catalog

401   for Southern California (1981 to June 2011), Bull. Seismol. Soc. Am., 102, 2239-

402   2244, doi: 10.1785/0120120010, 2012.

403   Helmstetter, A.: Is Earthquake Triggering Driven by Small Earthquakes?, Phys. Rev.

404   Lett., 91, doi: 10.1102/PhysRevLett.91.058501, 2003.

405   Helmstetter, A., Kagan, Y. Y. and Jackson, D. D. : Importance of small earthquakes

406   for stress transfers and earthquake triggering, J. Geophys. Res., 110, B05S08, doi:

407   10.1029/2004JB003286, 2005.

408   Kanamori, H. and Anderson, D. L.: Theoretical basis of some empirical relations in

409   seismology, Bull. Seismol. Soc. Am., 65, 1073-1095, 1975.

410   King, G. C. P., Stein, R. S. and Lin, J.: Static Stress Changes and the Triggering of

411   Earthquakes, Bull. Seismol. Soc. Am., 84, 935-953, 1994.

412   King, G. C. P. and Bowman, D. D.: The evolution of regional seismicity between

413   large earthquakes, J. Geophys. Res., 108, 2096, doi: 10.1029/2001JB000783, 2003.

414   Lin, J. and Stein, R. S.: Stress triggering in thrust and subduction earthquakes, and

415   stress interaction between the southern San Andreas and nearby thrust and strike-

416   slip faults, J. Geophys. Res., 109, B02303, doi: 10.1029/2003JB002607, 2004.

417   Lippiello, E., de Arcangelis, J. and Godano, C.: Role of Static Stress Diffusion in the

418   Spatiotemporal Organization of Aftershocks, Phys. Rev. Lett., 103, 038501, doi:

419   10.1103/PhysRevLett.103.038501, 2009.

420   Marsan, D. and Lengliné, O.: A new estimation of the decay of aftershock density

421   with distance to the mainshock, J. Geophys. Res., 115, B09302, doi:

422   10.1029/2009JB007119, 2010.

423   Miller, S. A., Collettini, C., Chiaraluce, L., Cocco, M., Barchi, M. and Kaus, B. J. P.:

424   Aftershocks driven by a high-pressure CO_2 source at depth, Nature, 427, 724-727

425   Mignan, A., King, G. C. P. and Bowman, D.: A mathematical formulation of

426   accelerating moment release based on the stress accumulation model, J. Geophys.

427   Res., 112, B07308, doi: 10.1029/2006JB004671, 2007.

428   Mignan, A.: Non-Critical Precursory Accelerating Seismicity Theory (NC PAST) and

429   limits of the power-law fit methodology, Tectonophysics, 452, 42-50, doi:

430   10.1016/j.tecto.2008.02.010, 2008.

431   Mignan, A.: Retrospective on the Accelerating Seismic Release (ASR) hypothesis:

432   Controversy and new horizons, Tectonophysics, 505, 1-16, doi:

433   10.1016/j.tecto.2011.03.010, 2011.

434   Mignan, A.: Seismicity precursors to large earthquakes unified in a stress

435   accumulation framework, Geophys. Res. Lett., 39, L21308, doi:

436   10.1029/2012GL053946, 2012.

437   Mignan, A.: Modeling aftershocks as a stretched exponential relaxation, Geophys.

438   Res. Lett., 42, 9726-9732, doi: 10.1002/2015GL066232, 2015.

439   Mignan, A.: Static behaviour of induced seismicity, Nonlin. Processes Geophys., 23,

440   107-113, doi: 10.5194/npg-23-107-2016, 2016a.

441 Mignan, A.: Reply to "Comment on 'Revisiting the 1894 Omori Aftershock Dataset

442   with the Stretched Exponential Function' by A. Mignan" by S. Hainzl and A.

443   Christophersen, Seismol. Res. Lett., 87, 1134-1137, doi: 10.1785/0220160110,

444   2016b.

445 Moradpour, J., Hainzl, S. and Davidsen, J.: Nontrivial decay of aftershock density

446   with distance in Souther California, J. Geophys. Res. Solid Earth, 119, 5518-5535,

447   doi: 10.1002/2014JB010940, 2014.

448 Ogata, Y.: Statistical Models for Earthquake Occurrences and Residual Analysis for

449   Point Processes, J. Am. Stat. Assoc., 83, 9-27, 1988.

450 Ogata, Y. and Zhuang, J.: Space-time ETAS models and an improved extension,

451   Tectonophysics, 413, 13-23, doi: 10.1016/j.tecto.2005.10.016, 2006.

452 Richards-Dinger, K., Stein, R. S. and Toda, S.: Decay of aftershock density with

453   distance does not indicate triggering by dynamic stress, Nature, 467, 583-586, doi:

454   10.1038/nature09402, 2010.

455 Ross, Z. E., Hauksson, E. and Ben-Zion, Y.: Abundant off-fault seismicity and

456   orthogonal structures in the San Jacinto fault zone, Sci. Adv., 3, doi:

457   10.1126/sciadv.1601946, 2017.

458 Seif, S., Mignan, A., Zechar, J. D., Werner, M. J. and Wiemer, S.: Estimating ETAS:

459   The effects of truncation, missing data, and model assumptions, J. Geophys. Res.

460   Solid Earth, 121, 449-469, doi: 10.1002/2016JB012809, 2017.

461 Shapiro, S. A. and Dinske, C.: Scaling of seismicity induced by nonlinear fluid-rock

462   interaction, J. Geophys. Res., 114, B09307, doi: 10.1029/2008JB006145, 2009.

463 Shaw, B. E. and Scholz, C. H.: Slip-length scaling in large earthquakes: Observations

464   and theory and implications for earthquake physics, Geophys. Res. Lett., 28, 2995-

465   2998, 2001.

466 Shearer, P. M.: Space-time clustering of seismicity in California and the distance

467   dependence of earthquake triggering, J. Geophys. Res., 117, B10306, doi:

468   10.1029/2012JB009471, 2012.

469 Toda, S., Stein, R. S., Richards-Dinger, K. and Bozkurt, S.: Forecasting the evolution

470   of seismicity in southern California: Animations built on earthquake stress transfer,

471   J. Geophys. Res., 110, B05S16, doi: 10.1029/2004JB003415, 2005.

472 Tormann, T., Wiemer, S. and Mignan, A.: Systematic survey of high-resolution b

473   value imaging along Californian faults: inference on asperities, J. Geophys. Res.

474   Solid Earth, 119, 2029-2054, doi: 10.1002/2013JB010867, 2014.

475 Utsu, T.: Aftershocks and Earthquake Statistics (1): Some Parameters Which

476   Characterize an Aftershock Sequence and Their Interrelations, J. Faculty Sci.

477   Hokkaido Univ. Series 7 Geophysics, 3, 129-195, 1970a.

478 Utsu, T.: Aftershocks and Earthquake Statistics (2): Further Investigation of

479   Aftershocks and Other Earthquake Sequences Based on a New Classification of

480   Earthquake Sequences, J. Faculty Sci. Hokkaido Univ. Series 7 Geophysics, 3,

481   197-266, 1970b.

482 Utsu, T., Ogata,, Y. and Matsu'ura, R. S.: The Centenary of the Omori Formula for a

483   Decay Law of Aftershock Activity, J. Phys. Earth, 43, 1-33, 1995.

484 van der Elst, N. J. and Shaw, B. E.: Larger aftershocks happen farther away:

485   Nonseparability of magnitude and spatial distributions of aftershocks, Geophys.

486   Res. Lett., 42, 5771-5778, doi: 10.1002/2015GL064734, 2015.

487 Varnes, D. J.: Predicting Earthquakes by Analyzing Accelerating Precursory Seismic

488   Activity, Pure Appl. Geophys., 130, 661-686, 1989.

489 Yamanaka, Y. and Shimazaki, K.: Scaling Relationship between the Number of

490   Aftershocks and the Size of the Main Shock, J. Phys. Earth, 38, 305-324, 1990.

491   Zaliapin, I., Gabrielov, A., Keilis-Borok, V. and Wong, H.: Clustering Analysis of

492   Seismicity and Aftershock Identification, Phys. Rev. Lett., 101, 018501, doi:

493   10.1103/PhysRevLett.101.018501, 2008.

494   Zaliapin, I. and Ben-Zion, Y.: Earthquake clusters in southern California I:

495   Identification and stability, J. Geophys. Res. Solid Earth, 118, 2847-2864, doi:

496   10.1002/jgrb.50179, 2013.

497

498   **Figures**
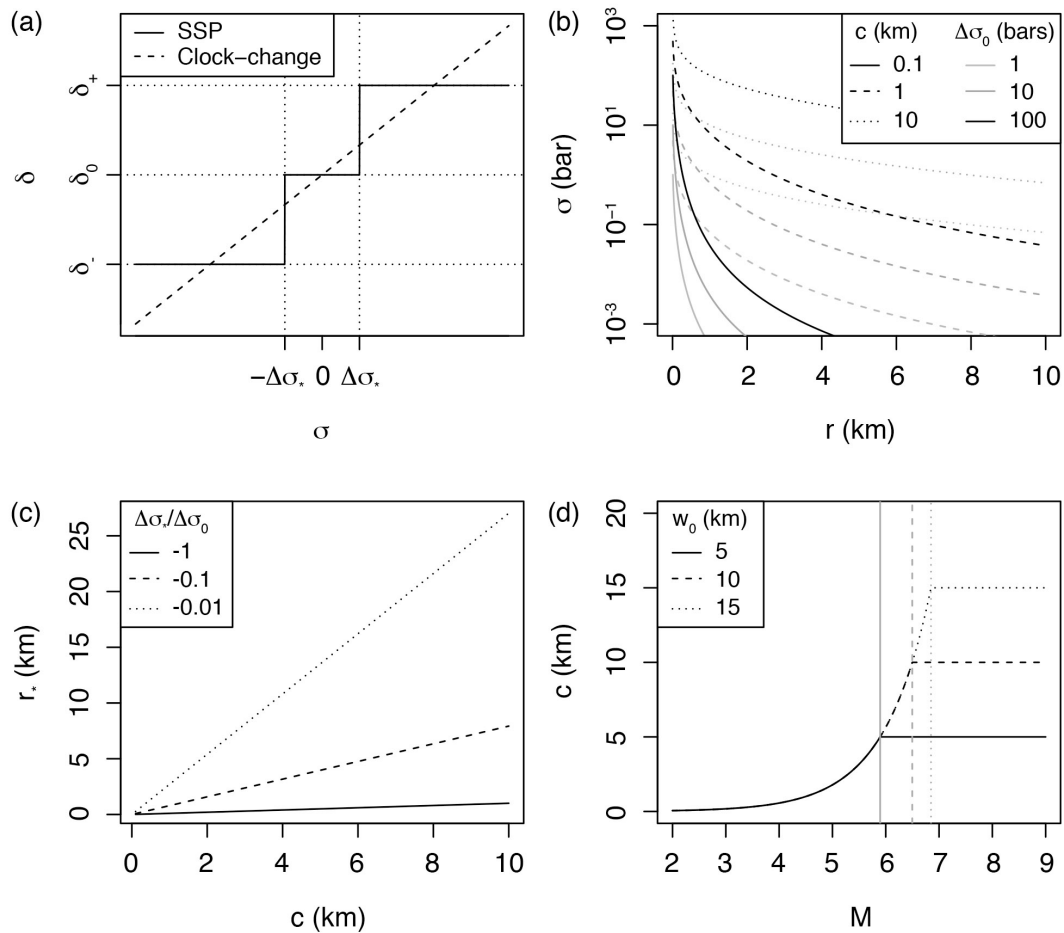
499

500   **Figure 1.** Definition of the aftershock solid envelope in a permanent static stress field:

501   (a) Event density stress step-function $\delta(\sigma)$ (Eq. 5) of the Solid Seismicity Postulate

502   (SSP) in comparison to the linear clock-change model; (b) Static stress σ versus

503   distance r for different effective crack radii c and rupture stress drops $\Delta\sigma_0$ (Eq. 6); (c)

504   Linear relationship between effective crack radius c and aftershock solid envelope

505   radius r_* for different $\Delta\sigma_*/\Delta\sigma_0$ ratios (Eq. 7); (d) Relationship between mainshock

506   magnitude M and effective crack radius c for different seismogenic widths w_0 (Eq. 8).

507
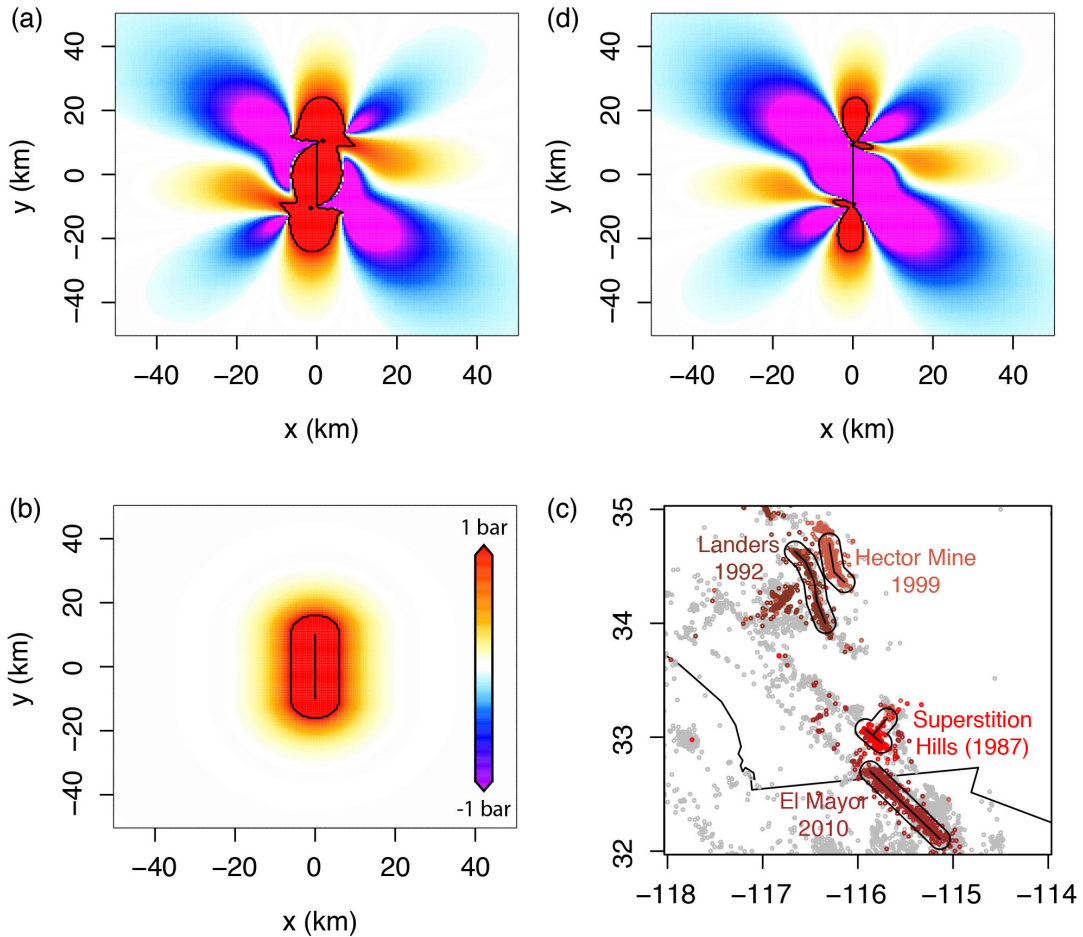
508

509   **Figure 2.** Possible static stress fields and inferred aftershock spatial distribution: (a)

510   Right-lateral Coulomb stress field for optimally oriented faults, where the mainshock

511   relieves all of the regional stresses $\sigma_r = 10$ bar, with $\Delta\sigma_0 \approx -Gs/L \approx$ - 10 bar ($G =$

512   $3.3.10^5$ bar the shear modulus, $s = 0.6$ m the slip, $L = 20$ km the fault length, and $w =$

513   10 km the fault width); (b) Radial static stress field computed from Eq. (6) with $\Delta\sigma_0 =$

514   -10 bar and $c = \sqrt{(Lw)/\pi}$ for consistency with (a); (c) Aftershock distribution of the

515   largest strike-slip events in the Southern California relocated catalog, identified here

516   as all events occurring within one day of the mainshock (see Data section 3.1); (d)

517   Right-lateral Coulomb stress field for optimally oriented faults, where the mainshock

518   relieves only a fraction of the regional stresses σ_r = 100 bar with $\Delta\sigma_0$ = -10 bar (same

519   rupture as in (a)) – The black contour represents 1 bar in (a), (b) and (d), and a 10 km

520   distance from rupture in (c). Coulomb stress fields of (a) and (d) were computed using

521   the Coulomb 3 software (Lin and Stein, 2004; Toda et al., 2005).

522
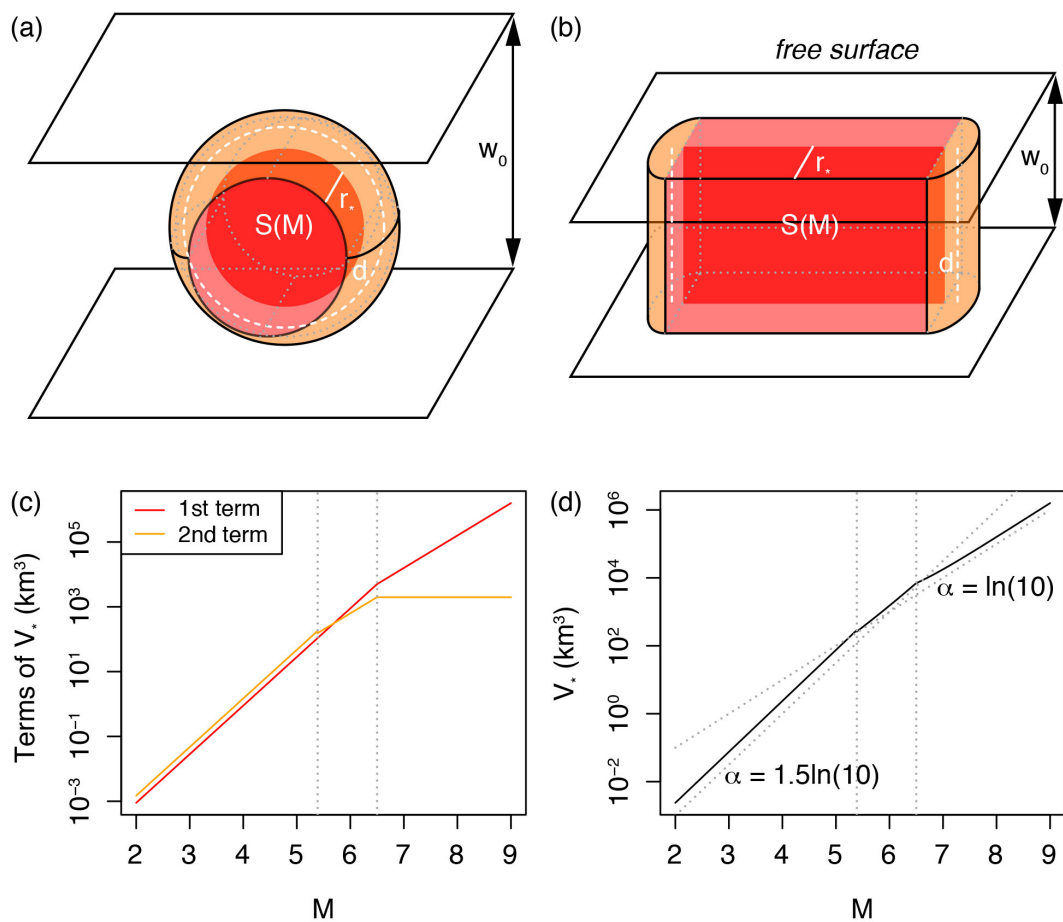
523

524   **Figure 3.** Geometric origin of the aftershock productivity law: (a) Sketch of the

525   aftershock solid for a small mainshock rupture represented by a disk; (b) Sketch of the

526   aftershock solid for a large mainshock rupture represented by a rectangle; (c) Relative

527   role of the two terms of Eq. (9), here with w_0 = 10 km and $\frac{\Delta\sigma_*}{\Delta\sigma_0}$ = -0.1 (to first estimate

528   c and r_* from Eqs. 8 and 7, respectively); (d) Aftershock productivity law (normalized

529   by δ_+) predicted by Solid Seismicity (Eq. 11). This relationship is of the same form as

530   the Utsu productivity law (Eq. 1) for large M (see text for an explanation of the lack

531   of break in scaling in Eq. 1 for small M). Dotted vertical lines represent M for

532   $c(M) + r_*(M) = \frac{w_0}{2}$ and $S(M) = \pi w_0^2$, respectively.

533
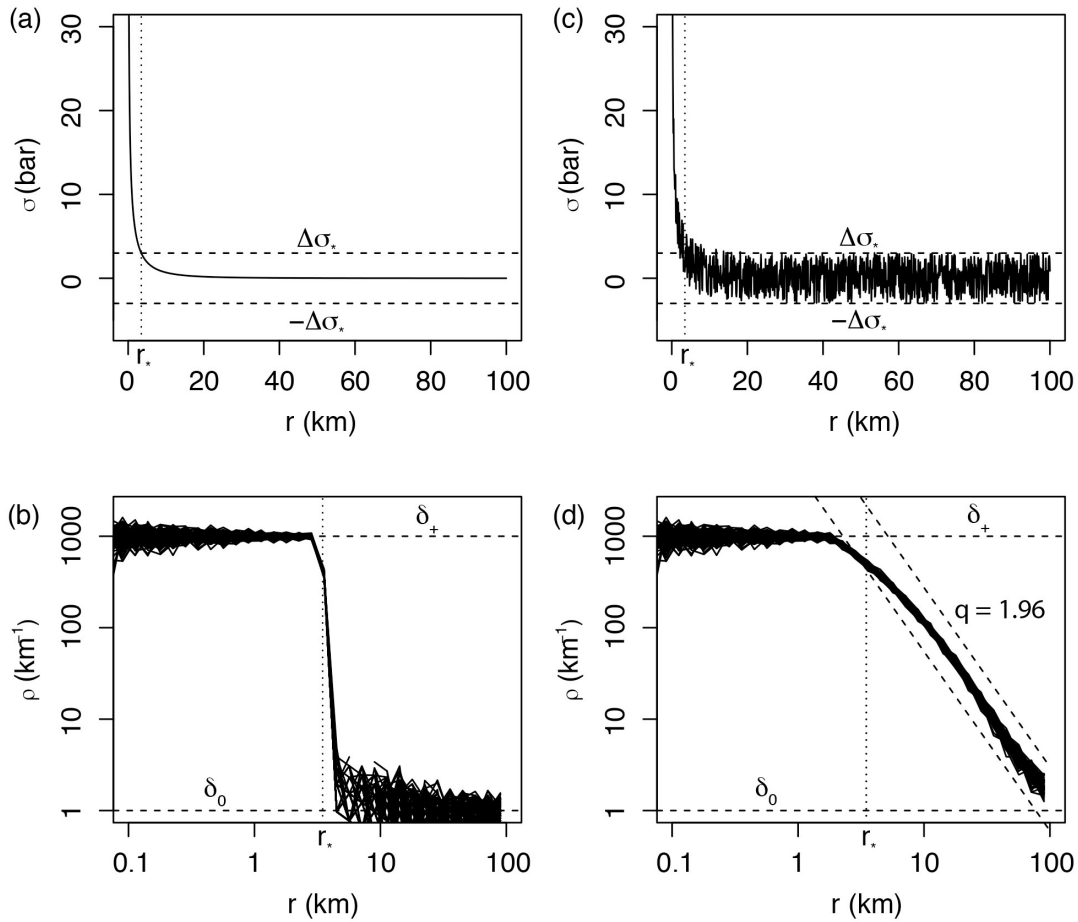
534

535   **Figure 4.** Spatial distribution of aftershocks following the SSP. (a) Smooth static

536   stress field as a function of distance r from the mainshock, with $\Delta\sigma_0 = $ -10 bar and $c = $

537   10 km (Eq. 6); (b) Step-like aftershock spatial linear density $\rho(r)$ with $\delta_+ = 1000$

538   events per km, $\delta_0 = 1$ event per km and $\Delta\sigma_* = $ -0.3$\Delta\sigma_0$ (*ad-hoc* ratio yielding $r_* = 3.5$

539   km; Eq. (7) – event distances sampled from the $\delta(r)$ distribution, repeated 100 times).

540   Such distribution is not observed in Nature; (c) Same as (a) but with random uniform

541 noise representative of spatial heterogeneities added to the regional stress field; (d)

542 Power-law-like aftershock spatial linear density ρ(r) with power exponent MLE

543 estimate q = 1.96, representative of real aftershock observations (see Fig. 5a), due to

544 the addition of uniform noise to the static stress field.

545
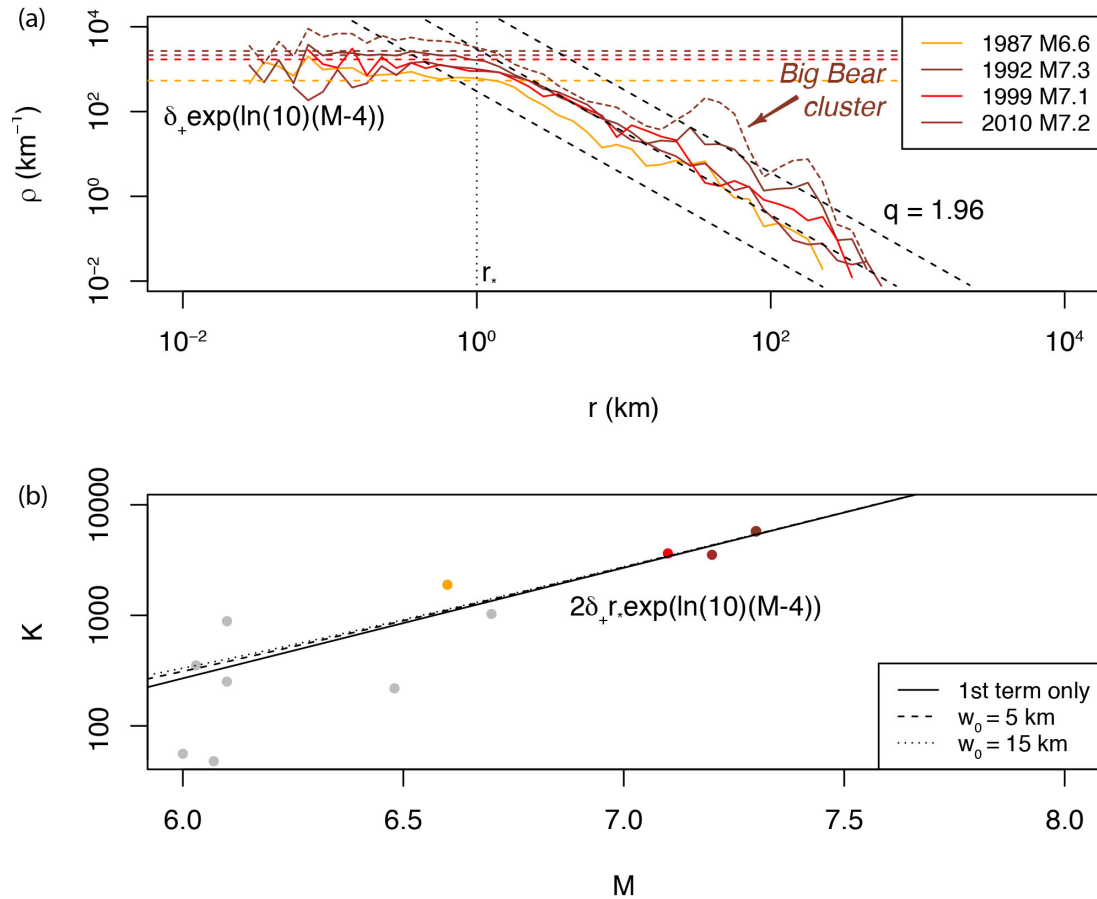
546

547 **Figure 5.** Estimating the Solid Seismicity parameters from the spatial distribution of

548 aftershocks: (a) Spatial linear density distribution ρ(r) of aftershocks for the four

549 largest strike-slip mainshocks in Southern California (with first-generation

550 aftershocks only; the density distribution comprising all aftershocks generated by the

551 Landers mainshock is represented by the dotted curve to illustrate the type of spatial

552 heterogeneity, such as the Big Bear cluster, not considered in the present study – see

553 also Fig. 2c). The Solid Seismicity parameters $r_* = 1$ km and $\delta_+(m_0 = 2) = 1.23$

554 events/km^3 can be retrieved from the observed plateau $\rho(r < r_*)$, in agreement with the

555 SSP (see Fig. 4d). Note that the spatial power-law decay at high r is similar to the one

556 expected by the SSP in the case of a static stress field with additive uniform noise

557 (expected $q = 1.96$ represented by the dashed black lines); (b) Aftershock productivity

558 K for $M > 6$. The curves represent the productivity law as defined by Solid Seismicity

559 (Eq. 17) for different w_0 values (first term only corresponds to $w_0 = 0$; Eq. 18).

560
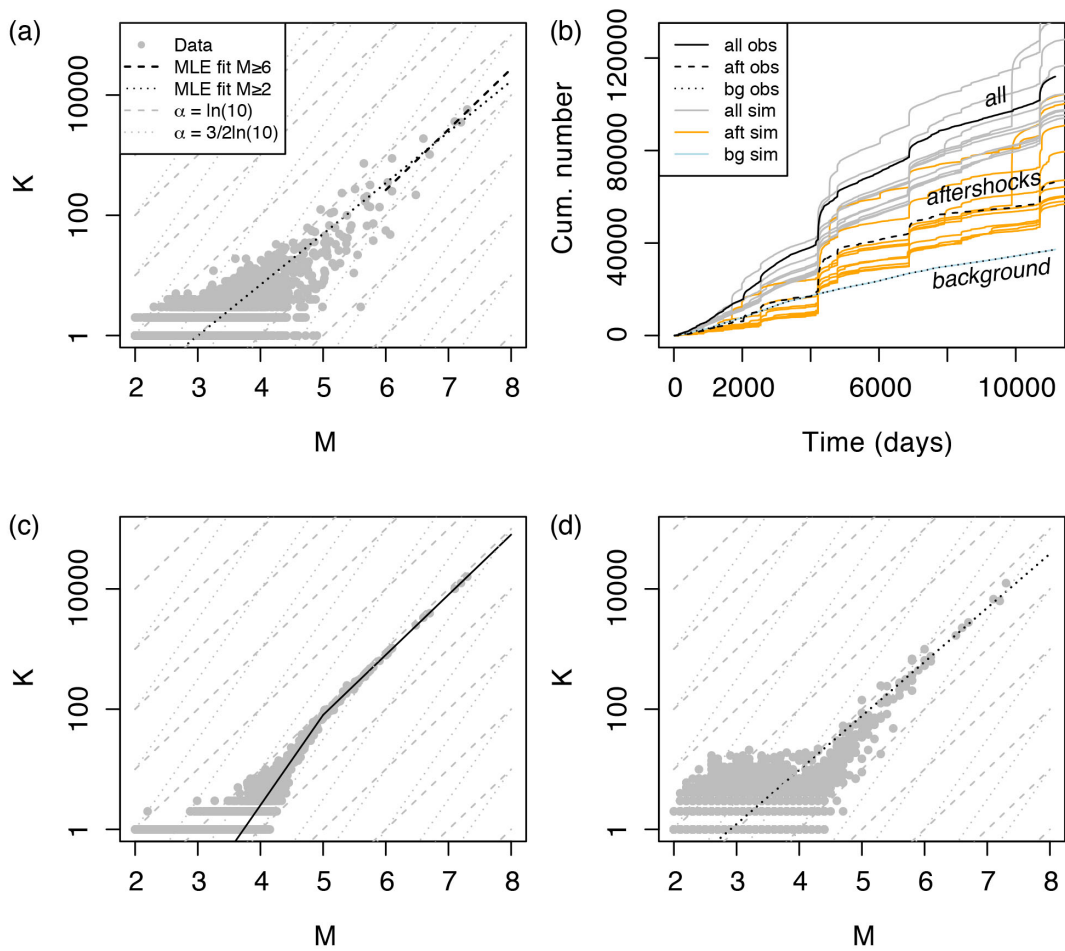
561

562 **Figure 6.** Aftershock productivity defined as the number of aftershocks $K(m_0 = 2)$ per

563 mainshock of magnitude M: (a) Observed aftershock productivity in Southern

564 California with aftershocks selected using the nearest-neighbor method; (b)

565 Seismicity time series with distinction made between background events and

566   aftershocks, observed ("obs", in black) and ETAS-simulated ("sim", colored); (c)

567   True simulated aftershock productivity with kink, defined from Eq. (20); (d)

568   Retrieved simulated aftershock productivity with aftershocks selected using the

569   nearest-neighbor method - Data points in (a), (c) and (d) are represented by grey dots;

570   the model MLE fits are represented by the dashed and dotted black lines for $M \geq 6$

571   and $M \geq m_0$, respectively; dashed and dotted grey lines are visual guides to $\alpha =$

572   3/2ln(10) and ln(10), respectively.

573